Photo-electrocatalytic performance of poly(3,4-ethylenedioxythiophene)/TiO2 nano-tree films deposited by oCVD/CVD for H2 production

Amr Nada, Maged Bekheet, Diane Samélor, Hugues Vergnes, Christina Villeneuve-Faure, Jim Cartier, Christophe Charmette, Sophie Tingry, Brigitte Caussat, Constantin Vahlas, et al.

Photo-electrocatalytic performance of poly(3,4-ethylenedioxythiophene)/TiO_2 nano-tree films deposited by oCVD/CVD for H_2 production

Amr A. Nada[a,b,c,d], Maged F. Bekheet[e], Diane Samélor[a], Hugues Vergnes[b], Christina Villeneuve-Faure[c], Jim Cartier[d], Christophe Charmette[d], Sophie Tingry[d], Brigitte Caussat[b], Constantin Vahlas[a] and Stéphanie Roualdes[d,*]

[a] CIRIMAT, Université de Toulouse, 4 allée Emile Monso, CS 44362, 31030 Toulouse Cedex 4, France.

[b] Laboratoire de Génie Chimique, Université de Toulouse, 4 allée Emile Monso, CS 84234, 31432 Toulouse Cedex 4, France.

[c] LAPLACE, Université Toulouse 3 - Paul Sabatier, 118 route de Narbonne - bât 3R3, 31062 Toulouse cedex 9, France.

[d] Institut Européen des Membranes, IEM, UMR-5635, Univ Montpellier, ENSCM, CNRS, Montpellier, France.

[e] Technische Universität Berlin, Faculty III Process Sciences, Institute of Material Science and Technology, Chair of Advanced Ceramic Materials, Straße des 17. Juni 135, 10623 Berlin, Germany.

* Corresponding author: stephanie.roualdes@umontpellier.fr

Keywords

CVD, PEDOT, TiO_2, photo-anode, water splitting, [211] anatase facet

Abstract

The hydrogen production from photo-electrocatalytic water splitting attracts extensive attention as a direct way to convert solar energy into chemical fuels. In this work, innovative photo-anodes composed of TiO_2 which has a preferable growth orientation [211] conjugated with PEDOT as bi-layers are prepared by a dry process strategy, combining oxidative and metalorganic chemical vapor deposition (CVD). Pure anatase, dendritic TiO_2 films of variable thickness are obtained at 500°C by varying the deposition time. Increase of films thickness from 474 to 2133 nm results in morphologies that evolve from dense and angular structures to isolated and nanostructured tree-like columns with a concomitant decrease of the

charge transfer resistance due to the enhancement of active facets of anatase structure. The PEDOT/TiO_2 bi-layer with an overall thickness of 1350 nm and a 50 nm thick upper-PEDOT layer exhibits the highest photocurrent response (0.26 mA cm^{-2} at 1.8 V/RHE), a fast photocurrent response under illumination, and the best hydrogen yield up to 4.1 µmol cm^{-2} h^{-1} with electronic conductivity being three order of magnitude higher than pristine TiO_2.

1. Introduction

Hydrogen is considered as a key energy carrier for the upcoming future, and significant efforts are underway to develop various technologies that require to maximize the yield of hydrogen production [1]. Green hydrogen produced from renewable sources plays an important role in the ecosystem for the limitation of CO_2 produced from diesel fuels [2]. Among the renewable sources, the sun and water make the photo-electro dissociation of water a promising technology for the production of green hydrogen. Several semiconductor materials have been considered as electrodes for water splitting such as cobalt-iron oxides, $BiVO_4$, Fe_2O_3, $LaFeO_3$, WO_3, $MnWO_4$, $ZnSnO_3$, ZnO and TiO_2 [3–8].

One of the most interesting materials for water oxidation is TiO_2 because it is environmentally friendly, inexpensive, and is chemically stable during oxygen evolution reaction. Nonetheless, TiO_2 is inactive under visible light due to its wide band gap and presents limitations for electron transfer. There are several progress tracks to overcome both drawbacks, such as the architectural design of TiO_2 lattice growth and/or the coupling with another photo-active material (semiconductor, non-metallic element, transition metal or lanthanide, and polymer) [9–13]. Indeed, the photoelectron-catalytic performance of TiO_2 depends on several architectural factors, such as its texture, crystal structure, composition, and morphology. For example, the growth lattice orientation is a key element [9,14,15], because the high-energy facets as [211] and [112] of TiO_2 are more efficient than the lowest-energy ones [101] for photocatalytic reactions [9,12]. All these architectural factors can be controlled and tuned by the preparation method of the electrode: anodization [16], reactive magnetron sputtering [17], atomic layer deposition (ALD) [18], electrospinning [19], sol-gel [20], or metalorganic chemical vapor deposition (MOCVD) [21]. We have recently shown that MOCVD, a dry deposition technique, allows producing tree-like column morphologies with high surface area to enhance the photocatalytic properties [14]. A complementary approach to improve hydrogen production is to combine crystallographically optimized TiO_2

(preferred orientation growth) with a conducting polymer such as polyaniline, polythiophene, and polypyrrole based on the inherent capacity of such polymers to transmit photo-generated charges [22]. The combination between TiO_2 and a conducting polymer can be considered as a p-n junction in which the polymer mostly acts as a p-type conductive material. This junction can enhance the lifetime between the electrons and holes in the photoelectrochemical cell (PEC cell) and also the band gap to be active under visible illumination [13].

Poly(3,4-ethylenedioxythiophene) (PEDOT) is one of the more promising conducting polymers since it has high electrical conductivity (up to ~ 8800 S cm^{-1} [23]), good environmental and mechanical stability and is optically transparent [24]. It is currently implemented in organic light-emitting diodes (OLEDs) [25], solar cells [26], fuel cells [27] and photodetectors [28]. Jian Liu et al. [29] successfully synthesized PEDOT/TiO_2 nanofibers, which showed a higher degradation efficiency of phenazopyridine as a pharmaceutical contaminant, suggesting the photo-degradation efficiency is influenced by the hole transfer from the TiO_2 to PEDOT. Katarzyna Siuzdak et al. [30] studied the highly stable organic-inorganic junction of TiO_2 nanotubes/PEDOT:PSS and obtained high photo-stability of the composite with 5 mA cm^{-2} under visible light attributed to the possibility of formation of a large p–n heterojunction. Bo Gao et al. [31] detected high performance of PEDOT photo-electrocatalytic for methylene blue degradation due to highly synergistic effects between photocatalysis and electrocatalysis. Shady Abdelnassera et al. [13] investigated the photo-electrocatalytic performance of PEDOT/TiO_2 nanotubes and then recorded significant increase in photocurrent response and lower charge transfer resistance compared to the pristine TiO_2 resulting from the heterojunction structure. PEDOT films are prepared by chemical oxidative polymerization in liquid solution [28], vapor phase processes (VPP) [32] and oxidative chemical vapor deposition (oCVD) [33]. Concerning the first process, unfortunately in the PEDOT:PSS solution growth, the hydrophobicity of the surface is substantial, leading to unavailable and complicated processing. There are many efforts to solve this issue of using PEDOT:PSS as plasma pre-treatment with oxygen on substrates or by using the captive bubble technique. But these approaches often damage substrate properties [34]. In another hand, VPP process suffers from critically relying on solvent casting of the oxidants. More interestingly, oCVD is a one-step dry technique using vapors of impurity-free monomer and oxidant as reactive species and requiring low thermal budgets [33]. Moreover, oCVD allows convenient control of thickness and thickness uniformity over large areas of PEDOT films [33].

In this work, we report the combination of TiO_2 and PEDOT as bi-layers targeting stability, integrity, and compactness of photo-electrochemical cells (PEC). A TiO_2 film is first processed by MOCVD at 500 °C from titanium tetra-isopropoxide (TTIP) and for different deposition times to obtain the preferable orientation lattice growth of TiO_2. Then a layer of PEDOT is deposited by oCVD on TiO_2 from EDOT and antimony pentachloride ($SbCl_5$) as monomer and oxidant, respectively. Preferential growth orientation, crystallites, micro-strain, and the lattice parameters are calculated from X-ray diffraction (XRD) by the Rietveld refinement calculation. The surface morphology and the growth rate of deposited films are investigated by field emission scanning electron microscopy (FESEM) and transmission electron microscopy (TEM). The conductivity and electrical properties are measured by conductive atomic force microscopy (C-AFM), and the surface roughness is investigated by AFM. Optical properties, i.e., the transmittance spectra and the band-gap, are measured by UV-vis spectroscopy. The facility of electron transfer and the lifetime between electrons and holes are investigated by electrochemical impedance spectroscopy (EIS). Finally, the photo-electro oxidation of water under visible light irradiation of the prepared photo-anodes is studied by detecting the amount H_2 evolution and calculating the Faradic efficiency.

2. Experimental

2.1. Materials and methods

A stainless steel cold wall MOCVD vertical shower reactor, detailed in [14] was used to process TiO_2 films at 500 ^{o}C. Ni foil (99.98%, Goodfellow), fused silica windows (Neyco), and Si (100) wafers (Neyco) were used as substrates. TTIP (99.999 vol.%, Sigma-Aldrich) was placed in a bubbler at 20.5 °C. Nitrogen (99.9999 vol.% Messer) was used as carrier and dilution gas with a flow rate fixed at 4.7 and 52.4 standard centimetres per minute (sccm), respectively. All lines of nitrogen gas were thermally controlled at 65 °C. The pressure during the deposition was fixed at 1 Torr. Different deposition times equal to 30, 45, 60, 85, and 135 min were implemented to obtain TiO_2 films with different thicknesses named T30, T45, T60, T85, and T135, respectively.

An horizontal, tubular, fuzed silica hot-wall oCVD reactor was used to deposit PEDOT films on the previously obtained TiO_2 ones. The reactor entrance was connected with three tubes carrying flowing gases, two of which were connected to microvalves and then to

jars placed in an oven, each jar containing the $SbCl_5$ (99 vol.%, Acros Organic) and 3,4-ethylenedioxythiophene (EDOT, 97 vol.%, Sigma-Aldrich) liquid reactants. Their temperature was fixed at 90 °C. The third line was N_2 (99.9999 vol.% Messer) with a continuous flow rate of 31.5 sccm. Deposition temperature was 140 °C and the deposition time was 5 min. The total pressure was fixed at 0.33 Torr. The PEDOT/TiO_2 bi-layers were named T30P, T45P, T60P, T85P and T135P films, respectively corresponding to T30, T45, T60, T85 and T135 TiO_2 films with an upper-layer of PEDOT.

2.2. Film characterization techniques

The crystal structure of the layers was investigated using Bruker-D8-GIXRD XRD diffractometer with the source of Cu Kα (λKαCu=0.154 nm) at 40 kV and 40 mA with a 0.066° step, step time of 2500 s. Rietveld refinement was performed on the diffraction patterns using the FULLPROF program [35] with the profile function 7 (Thompson-Cox-Hastings pseudo-Voigt convoluted with axial divergence asymmetry function) [36]. The films preferred orientation was determined with the March-Dollase model [37], as implemented in the FULLPROF program. The morphology and thickness of thin films were observed by using a Hitachi S4800 (Japan) field emission scanning electron microscope (FESEM). The conjugation of bilayers (PEDOT/TiO_2) and the distribution of elements were observed by Transmission electron microscopy (TEM) and Energy-dispersive X-ray spectroscopy (EDX) with a JEOL JEM 2100F microscope. The grid of TEM was prepared by a FEI Helios Nanolab600i dual beam focused ion beam (FIB) SEM. The ion column was 30 kV and the beam currents were between 47 nA and 15 pA. The protected film over the sample was composed of 2 layers based on carbon and platinum. The carbon film was deposited with thickness 200 nm over area of 20 μm × 2 μm. Then, a Pt layer of 3 μm thickness was deposited. The optical properties and the band gap of the films were detected from experimental UV-Vis spectra (Agilent-Cary 5000). The current versus voltage measurements at nanoscale were investigated by using C-AFM mode of an AFM Bruker Multimode 8 setup. Various negative DC voltages were applied on the backside of the sample, and the current was collected by a PtSi AFM-tip, which was in contact with TiO_2 or PEDOT/TiO_2 films surface (contact force around 50nN). PEDOT Film specific resistance, Rs [Ω cm^2], was detected with a Signatone S-302-4 four-point probe station on 2.5 × 2.5 cm^2 Pyrex substrates. A constant current of 200 nA was applied with a Keithley 6220 instrument, and the corresponding voltage was read on a Keithley 2182A one. The charge transfer resistance of the films was detected by EIS spectroscopy (Solartron SI 1260); the frequency

range was 0.01 Hz - 10^5 Hz with 0 mV or 10 mV AC amplitude. In addition to each prepared bi-layer used as photo-anode, a carbon glass (1 cm x 4 cm) as the cathode and a reference electrode Ag/AgCl (3 M KCl) SI Analytics (0.197 V vs. RHE) were immersed in the cell equipped with a quartz window and filled in with Na_2SO_4 0.1 M as the electrolyte (pH~6.5). The linear photocurrent-potential curves (LV) were measured in the same cell during the potential range 1 to 2 V/RHE with a scan rate of 10 mV/s, under dark or illumination with a Xenon lamp 100 W. The distance between the quartz window and the lamp was maintained at 10 cm. The chronoamperometric signal was detected at 1.8 V RHE for 1 hour under illumination. Finally, the hydrogen evolution was detected every 30 min by μGC (Agilent, 990 micro-GC) directly connected to the cell.

3. Results and discussion

3.1. Morphology

The thickness and the morphological evolution of the TiO_2 anatase films with deposition time was analyzed by FESEM. As shown in **Figure 1** and **Figure S1**, the thickness of the TiO_2 films increases linearly with the deposition time, resulting in a constant deposition rate of 15.8±0.6 nm/min. The T30, T45, T60, T85, and T135 films deposited on Ni foil have the following thicknesses: 474±30, 711±40, 940±30, 1350±50 and 2133±40 nm TiO_2. The thickness of the PEDOT upper layer is 50±10 nm, which is the same as logically obtained using a unique PEDOT deposition time.

It is also manifested from morphology observation of TiO_2 layers that the specific surface area of the thin films increases with increasing of the thickness of TiO_2 layers, as shown in [14], a previous study by our group. As shown in **Figure S1**, the structure of the tree-like column with inter-space between the columns has enhanced the surface area. As observed in **Figure 1**, the surface roughness of TiO_2 layers is directly proportional to their thickness due to the growing of columns structure. Furthermore, the decrease of the average arithmetic surface roughness Ra (which corresponds to the arithmetic average of the absolute values of the surface height over three different 10 μm x 10 μm surface areas) in presence of PEDOT compared to TiO_2 samples alone is noticeable only for TiO_2 layers surface roughness higher than 14 nm (T60, T85, T135). In contrast, no effect of PEDOT is observed on the surface roughness for the thinner TiO_2 layers having surface roughness lower than 14 nm (T30, T45) since, in this case TiO_2 is denser (like PEDOT) than columnar.

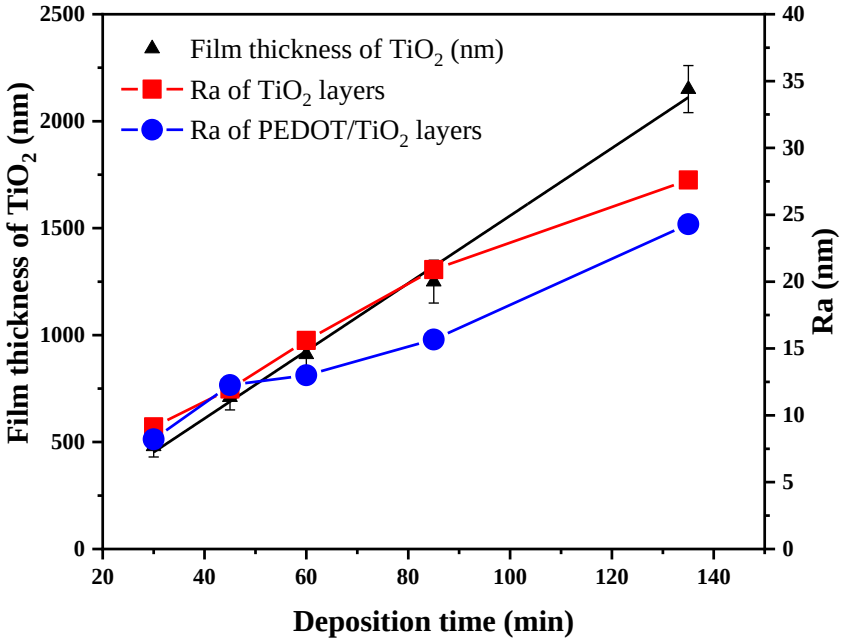

Figure 1. Evolution with the deposition time of the film thickness of TiO_2 layers and surface roughness Ra of all prepared thin films (investigated surface 10 µm x 10 µm).

Figure 2 (a-b) presents the FESEM images of cross-sectional and top-view of the T85 sample in which tree-like columns can be observed. The AFM topographic map (**Figure 2c**) shows a high grain size at such a long deposition time (85 min), which matches FESEM. Subsequently, the AFM analysis of T85P (**Figure 2d**) shows that T85P is smoother than T85 due to the presence of the PEDOT layer on the surface of TiO_2 layer. Indeed, the root mean square surface roughness is equal to 26 nm and 16 nm, over 10 µm x 10 µm surface, for T85 and T85P, respectively. Moreover, for a deeper description of the morphology and the elemental composition of T85P, the samples were investigated by TEM/STEM and EDX after preparing lamellas by FIB. The previously observed by FESEM tree-like columns morphology of T85P are displayed in the TEM and STEM micrographs of **Figure 2 (e-f)**. The EDX elemental composition mapping of T85P shows that the Ti element (**Figure 2-g**) is uniformly distributed in the tree-like columns. In addition, the uniform distribution of O element (**Figure 2-h**) with Ti elements is observed. Furthermore, sulfur (S), which participates in the thiophene ring of PEDOT is detected on the surface of the TiO_2 columns (**Figure 2-i**). It is worth noting the excellent conformity of the PEDOT layer on the TiO_2 rough surface. In addition, the presence of antimony (Sb) is detected as residual in the

PEDOT structure coming from the oxidizing agent $SbCl_5$ during the oCVD process (**Figure 2-j**). It was also observed on the surface of Ti and in the interspace between the columns, similar to the sulfur distribution, with some contamination of Sb over Ti coming from the FIB beam used during the preparation of grid. This specific configuration of the PEDOT/TiO_2 morphology should play an important role in the enhancement of the conductivity and photo-electrocatalytic performance, as will be described in the following sections.

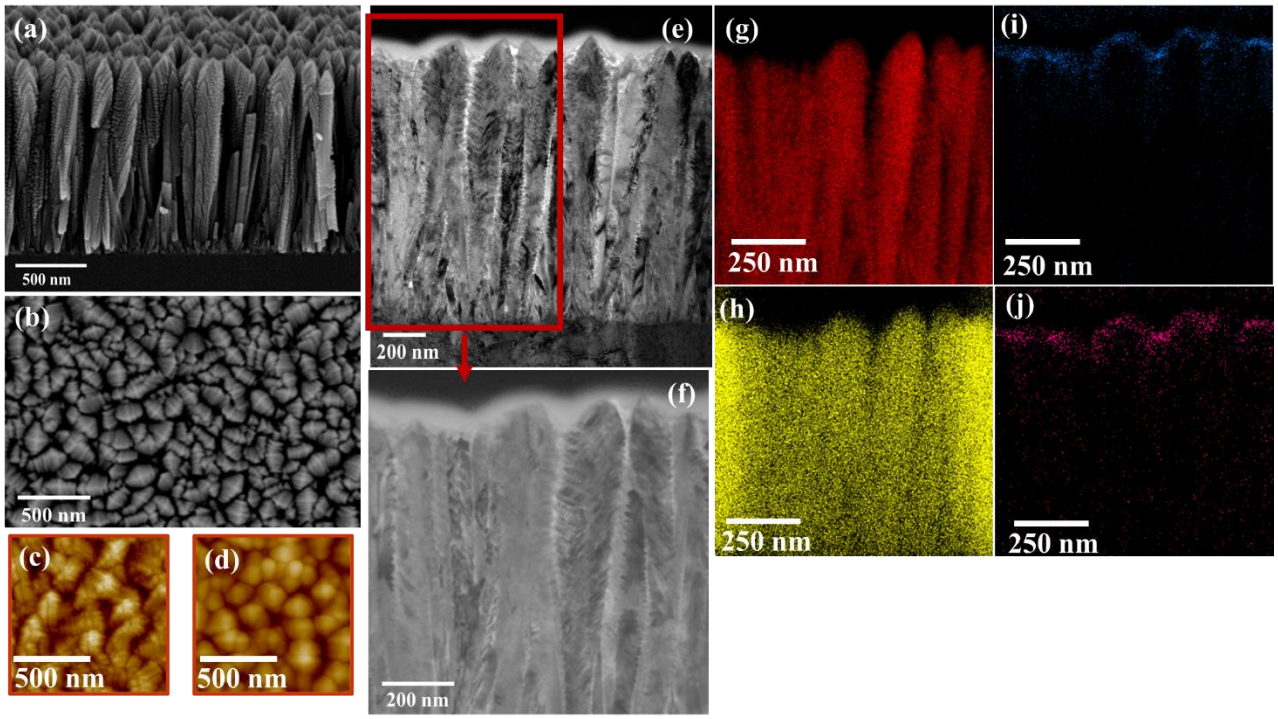

Figure 2. (a) SEM cross section of T85, (b) SEM top view of T85, (c, d) AFM topography of T85, T85P, respectively, (e, f) TEM and STEM of T85P, and (g) Ti, (h) O, (i) S, and (j) Sb EDX elements of T85P.

3.2. Crystallographic phase and texture

Figure 3 shows the XRD patterns of TiO_2 films deposited on Ni substrate at different thicknesses. All the peaks in the XRD patterns can be indexed to the anatase phase of TiO_2 (PDF Card #00-021-1272), and no other phase of TiO_2 has been observed. It can be seen that the intensities of XRD reflections corresponding to the TiO_2 phase are very low for the sample T30, indicating the small percentage of TiO_2 film on the surface of the Ni substrate. The intensity of XRD reflections corresponding to the TiO_2 phase increases with increasing the TiO_2 film thickness. Furthermore, the comparison of the intensities of XRD reflections

belonging to the TiO_2 phase in each film with those calculated for the reference anatase TiO_2 phase (PDF Card #00-021-1272) suggests a preferred orientation along the [112] and [211] directions in all samples (see **Figure 4b**).

XRD data were further analyzed by Rietveld refinement to gain more insight into lattice parameters, crystallite size, microstrain, and preferred orientation in the samples. **Figure S1** shows the observed, calculated, and difference profiles for the final cycle of the structure refinement of the T85 sample. The results of Rietveld refinement are given in **Table 1**. They show that the lattice parameters and unit cell volume of the anatase TiO_2 phase don't change significantly with increasing the TiO_2 thickness, which suggests the formation of a stoichiometric TiO_2 phase. In contrast, as shown in **Figure 4a**, the size of TiO_2 crystallites increases with thickness increasing while the microstrain decreases. The March-Dollase (MD) parameter *r* along the [112] and [211] directions were found to be less than unity in all samples. This MD parameter *r* defines the crystallites' distribution shape and is unity for an ideal random orientation (i.e., no preferred orientation), higher than one for needle-habit crystals and lower than one for platy crystals pack along the diffraction vector. Thus, the TiO_2 crystals have grown as plates along the [112] and [211] directions in all samples, suggesting that the increase of the TiO_2 thickness does not change the crystals of TiO_2 as well as the growth direction. However, as shown in **Figure 4c**, the degree of the preferred orientation η along the [112] and [211] directions, which is calculated from MD parameter *r* using the Zolotoyabko equation [38], is found to increase with increasing of the TiO_2 thickness. η indicates the percentage of excess crystallites with preferential orientation in comparison with randomly oriented crystallites in the film, which means that the T135 sample has crystallites with the highest total preferential orientation along the [112] and [211] directions. However, the T85 sample contains crystallites with a preferred orientation along [211] more intense than that of the T135 sample. Thus, high activity is expected for both T85 and T135 films as photo-anodes due to their enrichment in [211] facets (the key effect factor) that could destabilize the O_2p states on the surface and absorb the water molecules easily to improve the water splitting process [9,10].

As shown in **Figure S3**, no structural changes are observed in all samples after the deposition of the PEDOT layer on the surface of the TiO_2 one. This structural stability is attributed to the low deposition temperature of PEDOT (140°C).

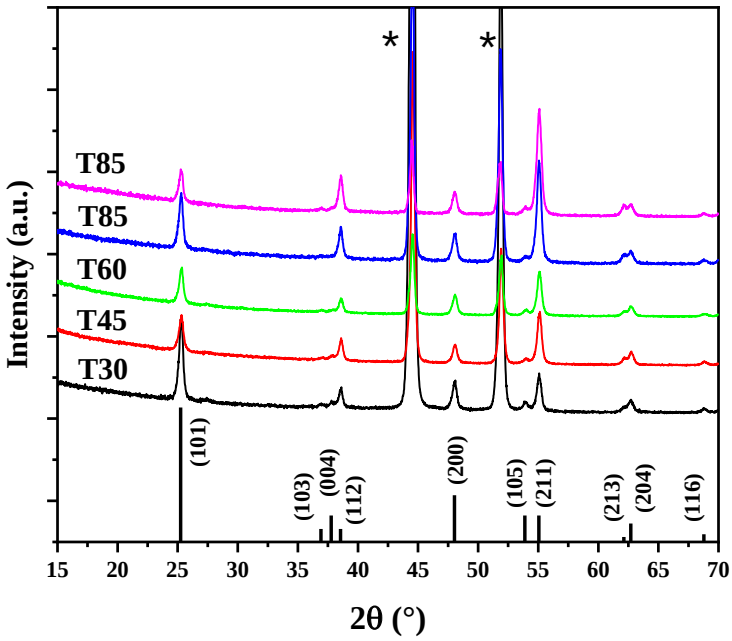

Figure 3. XRD patterns of T30, T45, T60, T85 and T135 samples. The calculated pattern of anatase TiO_2 (PDF Card #00-021-1272) is shown on the bottom. Star symbols refer to the corresponding reflections of metallic Ni (PDF Card #00-004-0850).

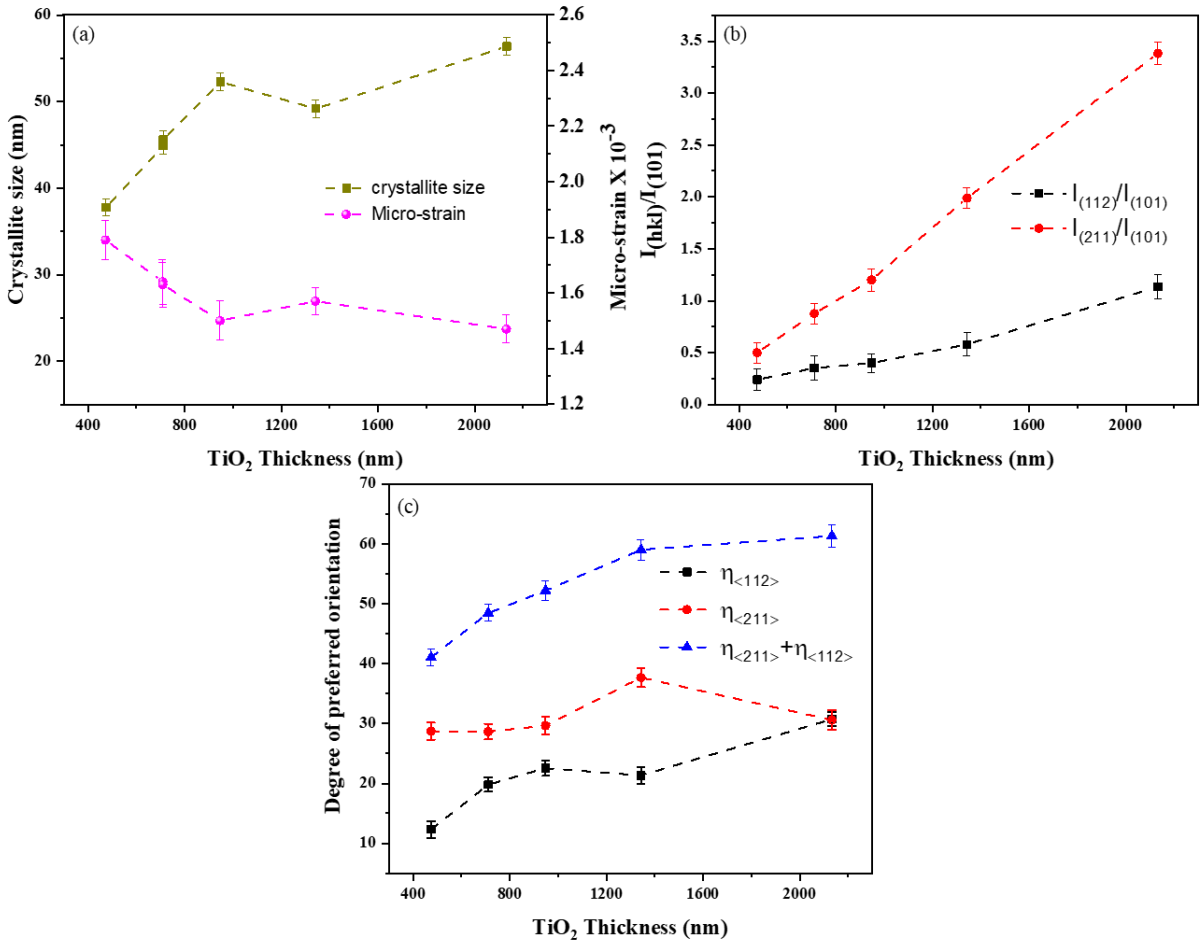

Figure 4: Thickness of TiO_2 dependence of (a) crystallite size and microstrain, (b) intensity ratio $I_{(112)}/I_{(101)}$ and $I_{(211)}/I_{(101)}$ and (c) degree of preferred orientation of anatase TiO_2 along (112) and (211) directions.

Table 1: Summary of structural parameters extracted from XRD patterns by Rietveld refinement of T30, T45, T60, T85 and T135 samples showing lattice parameters *a*, *b*, *c* [Å], the unit cell volume *V* [$Å^3$], crystallite size [nm] and microstrain and preferred orientation parameters obtained from March-Dollase (MD) model. *r*, *f* and η are March-Dollase parameter, the fraction of crystallites that are associated with a particular orientation axis and degree of preferred orientation, respectively.

Sample	Lattice parameter (Å)	Unit cell volume ($Å^3$)	Crys. size (nm)	Micro-strain x 10^{-3}	Preferred orientation parameters				
					(hkl)	$r_{(hkl)}$	$f_{(hkl)}$	$\eta_{<hkl>}$ (%)	η_{tot} (%)
T30	*a* = 3.7841(5) *c* = 9.5050(8)	136.10(2)	37.8(1.0)	1.79(7)	(112) (211)	0.37(1) 0.50(1)	0.24 0.76	12.32 28.72	41.04
T45	*a* = 3.7850(3) *c* = 9.5076(8)	136.21(4)	44.9(1.0)	1.64(8)	(112) (211)	0.38(1) 0.41(1)	0.39 0.61	19.80 28.65	48.45
T60	*a* = 3.7835(3) *c* = 9.5013(8)	136.01(2)	52.3(1.0)	1.50(7)	(112) (211)	0.41(1) 0.32(1)	0.48 0.52	22.54 29.65	52.19
T85	*a* = 3.7897(5) *c* = 9.5262(8)	136.81(2)	49.2(1.0)	1.57(5)	(112) (211)	0.34(1) 0.28(1)	0.39 0.61	21.33 37.68	59.02
T135	*a* = 3.7885(5) *c* = 9.5207(8)	136.65(3)	56.4(1.0)	1.47(5)	(112) (211)	0.33(1) 0.23(1)	0.55 0.45	30.72 30.59	61.31

3.3. Optical properties

The absorbance spectra of the TiO_2 and PEDOT/TiO_2 films deposited on quartz substrates were recorded for samples of various TiO_2 thicknesses (**Figure 5a**). The TiO_2 films have a transmittance in the visible range of around 40 to 80%, depending on the TiO_2 thickness. However, it slightly decreases in the presence of PEDOT. In addition, the absorbance increases as the layer thickness increases from 475 up to 2135 nm. This is a consequence of the light scattering, which increases with the surface roughness resulting from the increase in grain size. The optical band gap (E_g) of the films was calculated from absorbance spectra (**Figure 5b**) using the Kubelka-Munk remission function according to the following equation [1,39]:

$$\alpha h\nu = A(h\nu - Eg)^2 \quad \text{Equation (1)}$$

where α is the absorption coefficient, ν is the light frequency, and E_g is the indirect transition band gap. The optical band gap decreases from 3.32 to 2.71 eV, with the TiO_2 thickness increasing from 475 to 2135 nm respectively, as observed in **Figure 5b**. Sarantopoulos observed the same effect on anatase TiO_2 MOCVD films of variable thickness [40], and Pankaj Tyagi et al. for zinc iodide, ZnI_2 films [41]. In addition, the preferable orientation should also affect the band gap [42]. So, the thicker samples have lower band gaps due to the

growth orientation effect and their unique morphology. In another hand, the bi-layers of PEDOT/TiO_2 have lower band gaps than pure TiO_2 thin films. Indeed, the range of band gaps in TiO_2 layers is 3.32 to 2.71 eV for T30 to T135 samples, whereas it decreases to 3.3 - 2.48 eV for T30P to T135P films, respectively. The enhancement of optical properties in the presence of PEDOT can be explained by the fact that the energy levels of PEDOT (the highest occupied molecular orbit (HOMO) and the lowest unoccupied molecular orbit (LUMO)) are higher than the energy levels of TiO_2 (the conduction band (CB) and valence band (VB)), respectively [13]. PEDOT acts as a hole transport layer and increases the lifetime between the electrons and holes in the bilayer. There is a synergetic effect between PEDOT and TiO_2 to capture a larger number of photons than pure TiO_2, as already observed by Abdelnasser et al [13].

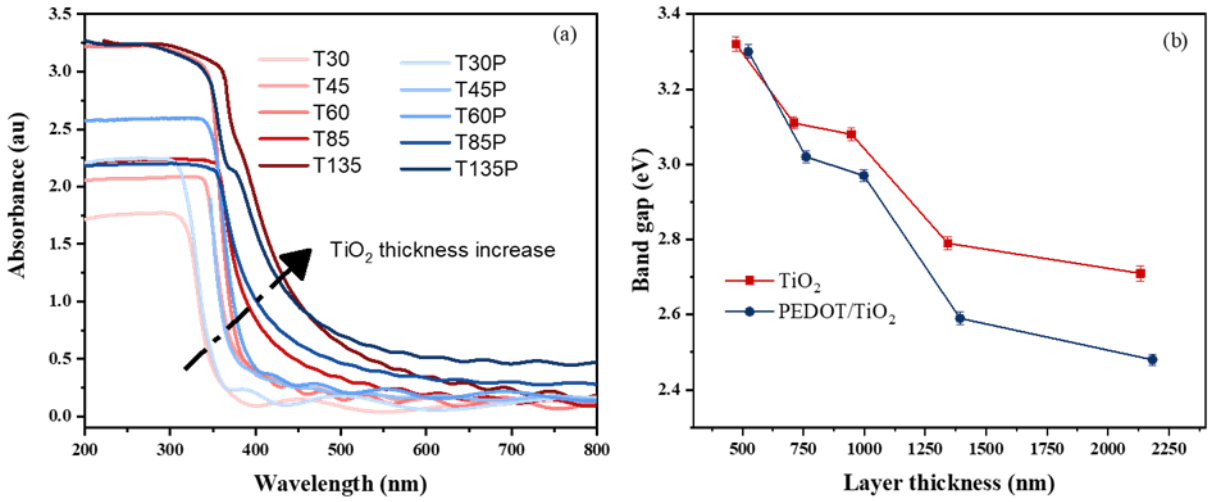

Figure 5. (a) Absorbance spectra of pure TiO_2 and PEDOT/TiO_2 films, (b) Variation of the bandgap of TiO_2 and PEDOT/TiO_2 films versus the TiO_2 layer thickness.

3.4. Nano-scale conductivity properties

To investigate conduction mechanism at nanoscale and compare it to TiO_2 and PEDOT/TiO_2 morphology, C-AFM measurements have been performed. The C-AFM topography and current maps and the related occurrence diagram of the T85 and T85P films are presented in **Figures 6a to 6f**. Considering the bare TiO_2 films, the conduction occurred through grain as highlighted by the comparison of the topography (**Figure 6a**) and the current (**Figure 6b**) maps. Indeed, the non-conductive areas are light and the most conductive areas

(negative current) are the darkest areas. A different behavior is observed for the PEDOT/TiO_2 films. Indeed, the current flow is no more associated to grains as the latter are not visible through the PEDOT layer (**Figures 6d and 6e**). Moreover, it can be noted another broad difference between the T85 and T85P samples in term of current magnitude. Indeed, the current in T85P is three order of magnitude higher than in T85 (nano- versus pico-ampere), whereas the applied voltage is two order of magnitude higher for T85. Such current increase is attributed to the presence of the conductive polymer (PEDOT) on the surface of T85P. It is worth noting that the conductivity of PEDOT film was determined to be 530±23 S/cm^2 using a four-probe method. The occurrence diagrams (**Figures 6c** for T85 and **6f** for T85P) present the statistical distribution of the current, for a fixed applied voltage. 100% of the surface of sample T85 is conductive and two different conductive areas are observed. Grains present a medium range current (area B) whereas the current is higher among grains (area C). However, such slight current increase among grains is an artefact due to the increase of current surface collection when the tip is in the depression between grains. 90% of the surface of sample T85P is conductive and three different conductive areas are observed: non-conductive area (zone A) and various range current areas (regions B and C). **Figures 6g and 6h** compare the conduction properties of TiO_2 and PEDOT/TiO_2 films through the evolution of the current as function of the electric field (i.e. applied voltage divided by film thickness). For pure TiO_2 thin films, the current increases with the increase of film thickness due to the prevailing columnar morphology that facilitates the transport of electrons [15]. This phenomenon disappears in case of PEDOT/TiO_2 films where PEDOT enhances the conductivity and probably decreases the charge collection barrier. **Figure 6g** also indicates a variation of the electric field conduction threshold depending on the thickness of the pure TiO_2 films. We attribute such threshold modification to two factors, (i) the decrease of the band gap with increasing the thickness of the film **(Figure 5)**, thus facilitating electron transfer from TiO_2 to the PtSi AFM tip, (ii) and the predominance of high surface energy (211) facets with increasing thickness [9]. In contrast, no electric field threshold is observed for the PEDOT/TiO_2 bi-layer. This is consistent with the fact that the PEDOT layer between the AFM-tip and TiO_2 favors the electron transfer.

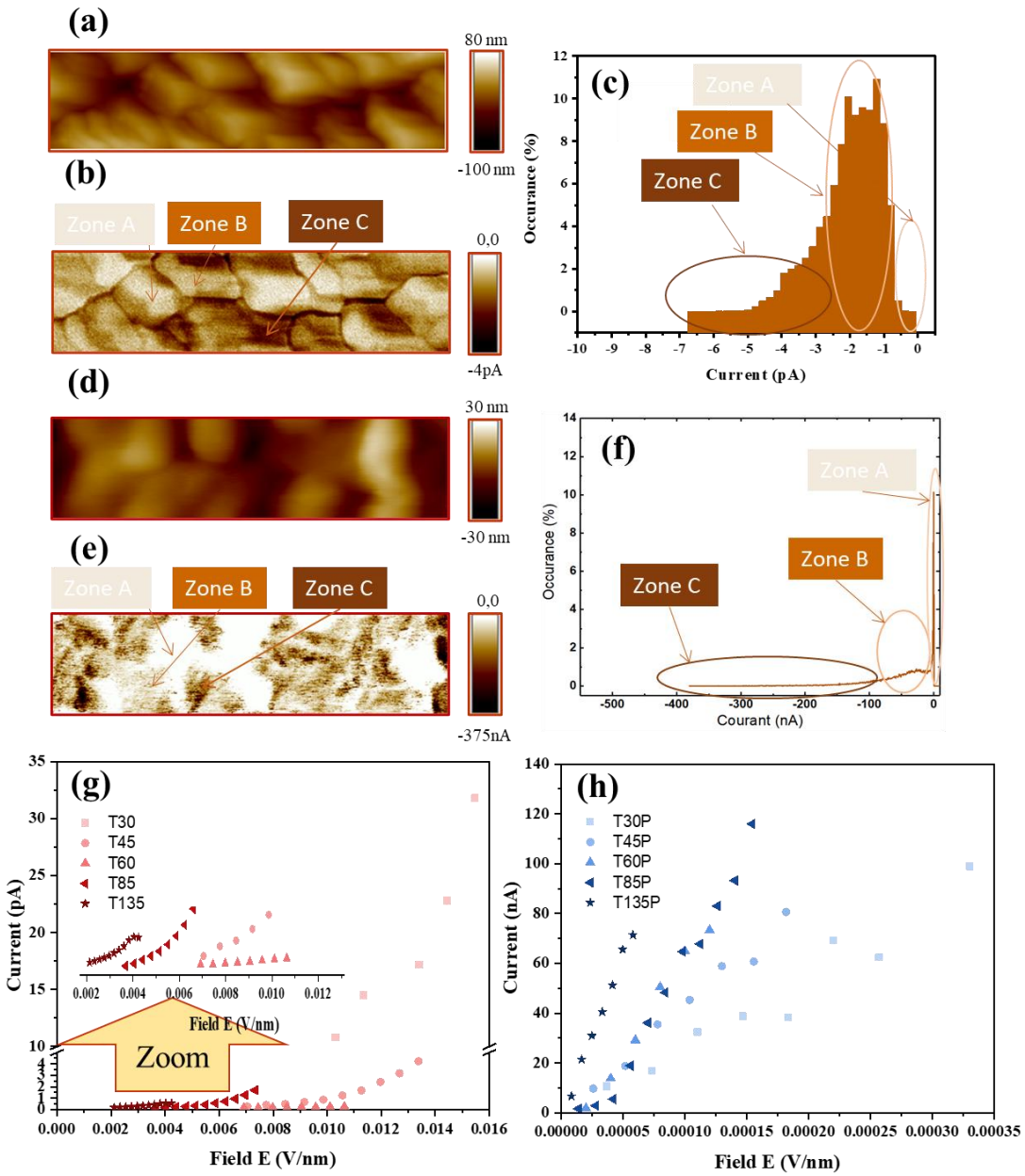

Figure 6. (a, b and c) Topography, current maps, and corresponding occurrence diagram of T85 thin film, respectively at bias voltage of – 9.5 V. (d, e and f) Topography, current maps, and corresponding occurrence diagram of T85P thin film, respectively at bias voltage of – 120 mV. (g) C-AFM current versus applied electric field curves of TiO_2 films and (h) C-AFM current versus applied electric field curves of PEDOT/TiO_2 bi-layers.

3.5. Charge transfer

The electrochemical impedance spectroscopy analysis (EIS) was performed to observe the electrons separation efficiency and determine their lifetime stability. The Nyquist EIS curves of TiO_2 films and PEDOT/TiO_2 bi-layers are shown in **Figure 7 (a,b),** and Bode phase EIS curves are shown in **Figure S3**. Herein in Nyquist plot, the semicircle diameter decreases with increasing the TiO_2 film thickness, indicating the reduction in the resistivity of the interface between films and electrolyte. This observation is in accordance with the C-AFM results showing the charge transport electric field threshold decrease with the increasing of the TiO_2 thickness, thus facilitating electrons collection and transport. Moreover, the semicircle diameter of EIS decreases under illumination when compared to the dark due to the enhancement of electrons transfer under light, leading to the decrease of TiO_2 films charge transfer resistance [43]. The resistivity has been quenched to half in the case of PEDOT/TiO_2 bilayers when compared to the TiO_2 bare films, which means that the bilayer structure provides more favorable charges mobility and separation [13]. This observation is also in agreement with C-AFM measurements. Furthermore, the bode-phase peak moves to a lower frequency range with increasing the TiO_2 thickness, especially in the presence of PEDOT (**Figure S4)**, which indicates the improvement of the lifetime between electrons and holes under illumination [1]. The lifetime of the electrons before recombination calculated from the equation (ES1) [1] is presented for all samples in **Figure 7d**. We can observe the linearity of the electrons' time stability and a noticeable effect of PEDOT addition for T60, T85 and T135 films, which indicates that the most convenient TiO_2 films are those having a thickness higher than ~ 1 µm, as observed from the surface roughness investigation (**Figure 3)**. For such films, the TiO_2 columnar structure leads to better electrons' stability than the dense structure but with limitation of conductivity; herein, the thin layer of PEDOT plays an important role in the improvement of the conductivity and in the stability of electrons as observed in terms of lifetime stability (**Figure 7d)**. Additionally, the cyclic voltammetry (CV) of the film in the range of non-faradic reaction (+0.1 to +0.3 V vs RHE) (**Figure S5**) at different scan rates was used to measure the capacitance double layer (C_{dl}) [2]. The current values obtained from the CV curves (equation ES2) were used as a function of the scan rate to calculate $C_{dl,}$ deduced from the slope (**Figure 7c**) [2]. The C_{dl} values, presented in **Figure 7d**, increase from 0.14 to 0.85 µF cm^{-2} with the TiO_2 thickness increasing from 0.48 to 2.13 µm, which indicates an enhancement of the electrochemical active surface area (EEASA). Indeed the capacitance double layer and the electrochemical active surface area (EEASA) are proportional [44]. In addition, the presence of PEDOT improves the C_{dl} values, especially for

the thicker TiO_2 layer from 0.11 up to 1.03 µF cm^{-2} for both extreme films T30P and T135P films, respectively.

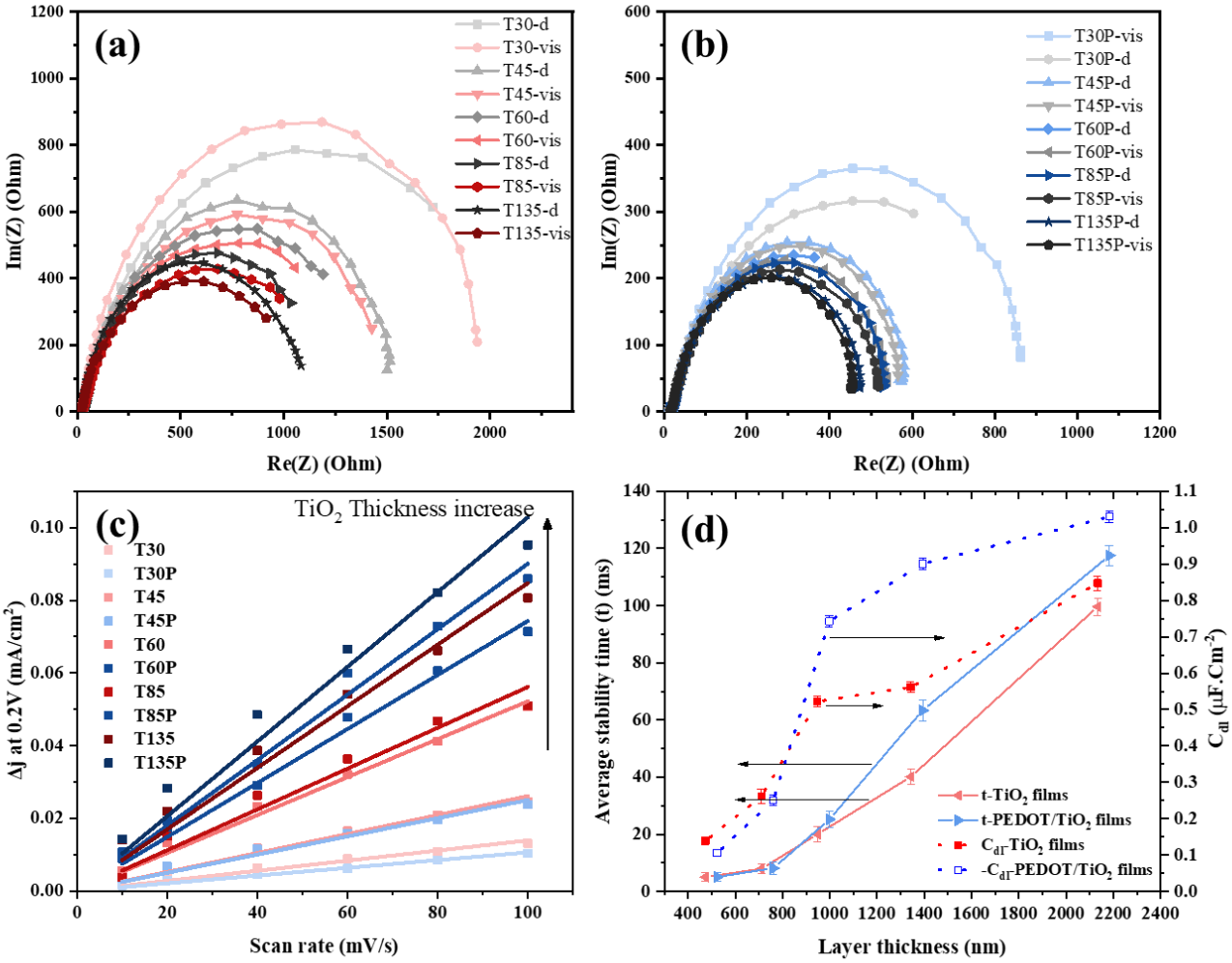

Figure 7. (a, b) EIS Nyquist plots in a frequency range of 0.1 Hz to 1 MHz of TiO_2 and PEDOT/TiO_2 films, respectively. (c) The current density variation (Δj=(ja-jc)/2), at 200 mV vs. RHE; data obtained from the CV in Figure S4 against scan rate to fit a linear regression. (d) C_{dl} and electron lifetime stability as a function of thickness for all films.

3.6. Photo-electrocatalytic properties and hydrogen evolution

The photoactivity of TiO_2 and PEDOT/TiO_2 films was depicted in the oxygen evolution reaction (OER) range (from 1 to 2 V vs. RHE) in the dark and under illumination as

presented in the linear voltammetry curve (**Figure 8 (a, b)**) using the three electrodes system. The behavior of TiO_2 films clearly improves with increasing thickness and in the presence of PEDOT, especially for T85P and T135P; the largest integral area of both meaning highest real capacitances [43]. The linear voltammetry curve (LV) at this potential range displays that the films are oxidatively stable due to many factors, such as the growth in a preferred orientation along the [112] and [211] directions depicted from XRD, morphological structure observed from TEM, and the improvement of electron transfer previously depicted from C-AFM and EIS. The LV of preferred orientation along the [112] and [211] directions of prepared photo-anodes was a proof of better performance than P25 (benchmark photo-anode). Interestingly, the highest (photo)current density was obtained for the T85P electrode in the dark and under light illumination (0.92 and 1.26 mA cm^{-2} at 2 V vs. RHE) with quite the same performance for T135P (0.86 and 1.22 mA cm^{-2} at 2 V vs. RHE), respectively. This higher photocurrent density refers to the ability of light harvesting and the narrow distance between the valence and conduction bands, as confirmed by band gap calculation and the transmittance spectra. The chronoamperometric response for one hour under illumination and at a fixed potential 1.8 V vs. RHE (**Figure 8c**) shows a slight current attenuation of 5% after 10 min of continuous testing, which can be attributed to the stability of these electrodes for water splitting under these conditions. To study hydrogen evolution of the T85 and T85P photo-anodes, the gas production measurements were implemented for 2 h in the PEC. In **Figure 8d**, it can be noted that the evolution rate of hydrogen on glassy carbon under illumination is twice higher in the presence of PEDOT (T85P) than for bare TiO_2 (T85) after 120 min. The corresponding yield of hydrogen production for T85P reaches 4.05 µmol cm^{-2} h^{-1}. This improvement related to the PEDOT addition can be attributed to the decrease in the resistivity of T85P, facilitating electrons transfer and increasing electrons lifetime beside the narrow band gap that was observed by EIS and transmittance spectroscopy measurements. The mean faradic efficiency (FE) values were calculated from the µGC and chronoamperometric results. The FE values were 75 and 81% for T85 and T85P, respectively. The higher faradic efficiency is attributed to the higher photocurrent density detected from chronoamperometric and LVS measurements. The hydrogen yield obtained in this work is competitive with other TiO_2 photo-electrodes reported in previous studies (Table 2), such as that from Kawrania et al., who recorded a H_2 yield of around 1 µmol cm^{-2} h^{-1} with a calcium copper titanate photoanode (CCTO perovskite) exposed under visible light, and of 2.5 µmol cm^{-2} h^{-1} after modification of CCTO with copper oxide over its surface [45]. The hydrogen production measurement was performed in three cycles with each cycle lasting 2 h,

as shown in **Figure 8e** proving that the hydrogen production was linear and stable during these cycles.

Table 2: Hydrogen efficiency density of various studied materials in literature.

Materials	Light source	H_2 (µmol cm^{-2} h^{-1})	FE (%)	References
$CaCu_3Ti_4O_{12}$	Linear halogen lamp 150 W	1	73	[45]
CuO/ $CaCu_3Ti_4O_{12}$	Linear halogen lamp 150 W	2.5	79	[45]
TiO_2 rutile doped B-N	Xe lamp 300 W	3.73	--	[46]
Cu_2S-TiO_2/TiO_2 NPs	White light illumination 100 W	55	--	[47]
PEDOT-Pt-TiO_2_10% (photocatalysis)	Xe lamp 1000 W	$1.51 * 10^{-3}$	--	[48]
PEDOT/TiO_2	Xe lamp 100 W	4.05	81	This work

The photo-electrochemical processes with the energy levels for T85P are depicted in **Figure 9** in accordance with the findings mentioned above where it was aligning the conduction band (CB) and valence band (VB) of T85 depending on the following equations [49]:

$$E_C - E_C^{bulk} = \frac{m_h}{m_{e^+} m_h} X\ (E_g - E_g^{bulk}) \qquad \text{Equation (2)}$$

$$E_V - E_V^{bulk} = -\frac{m_e}{m_{e^+} m_h} X\ (E_g - E_g^{bulk}) \qquad \text{Equation (3)}$$

Where, E_C^{bluk}, E_V^{bluk} are -0.6, 2.6 eV of anatase with band gap (E_g^{bluk}) 3.2 eV [50]. The mass of electrons (m_e) and the mass of holes (m_h) are 0.0948, 0.1995 m_0 of anatase [51]. In our work, the E_g is 2.79 eV of T85, so E_C and E_V are -0.32 and 2.47 eV vs. NHE, respectively.

The HOMO of PEDOT (prepared via oCVD) is 0.45 eV vs. NHE, where PEDOT acts as a hole transport layer [52]. It improves the efficiency of the T85P photo-anode. Additionally, PEDOT plays a crucial function in lowering the rate of e^-/h^+ recombination.

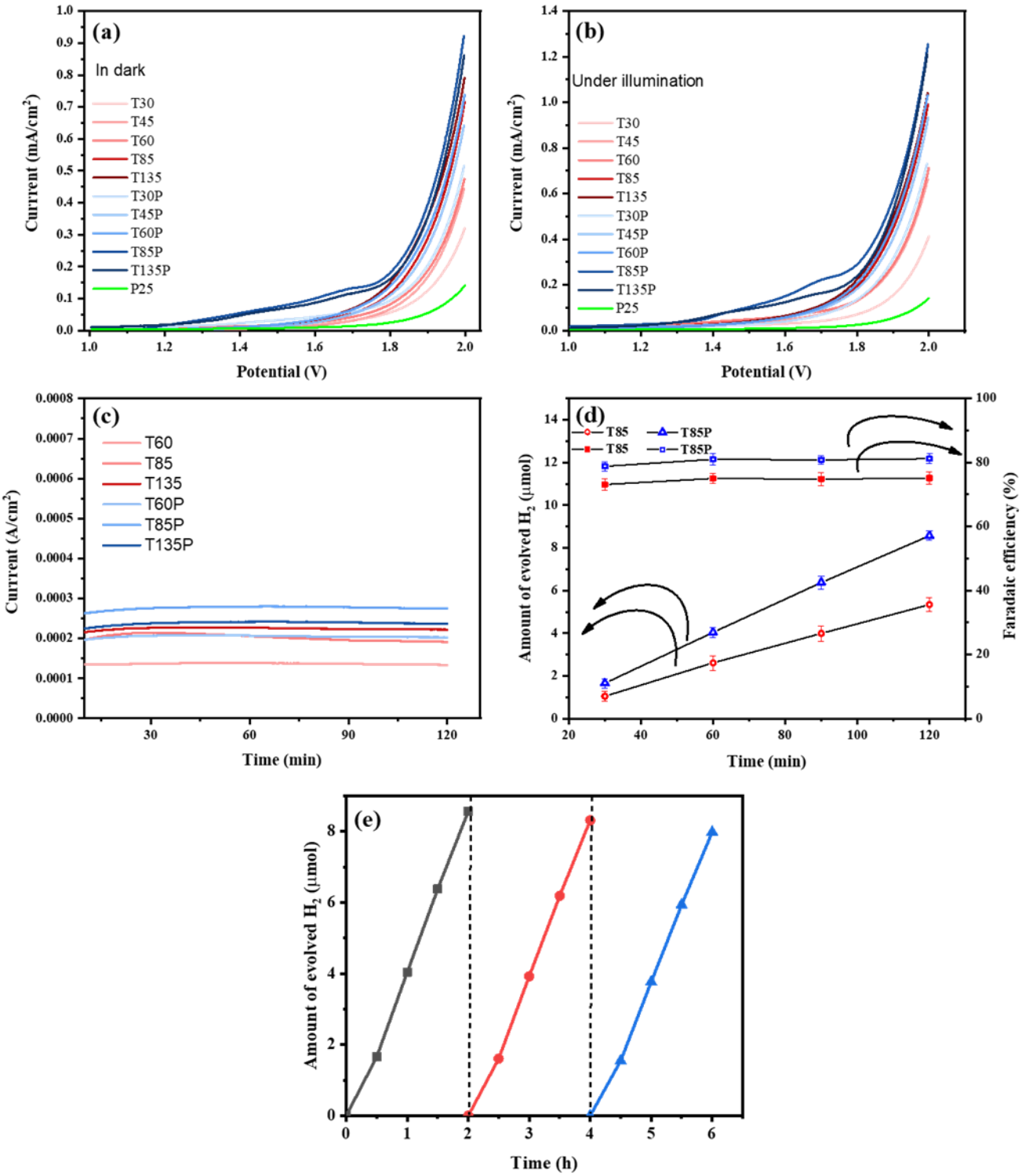

Figure 8. OER-LV curves of TiO_2 and PEDOT/TiO_2 in the dark (a) and under illumination (b) in 0.05 M Na_2SO_4 vs Ag/AgCl. (c) Chronoamperometry measurement of TiO_2 and PEDOT/TiO_2 films under illumination. (d) Quantity of detected hydrogen and faradic efficiency for T85 (blue symbols) and T85P (red symbols) samples. (e) Reusability of T85P for photo-electrochemical H_2 production activity under visible light.

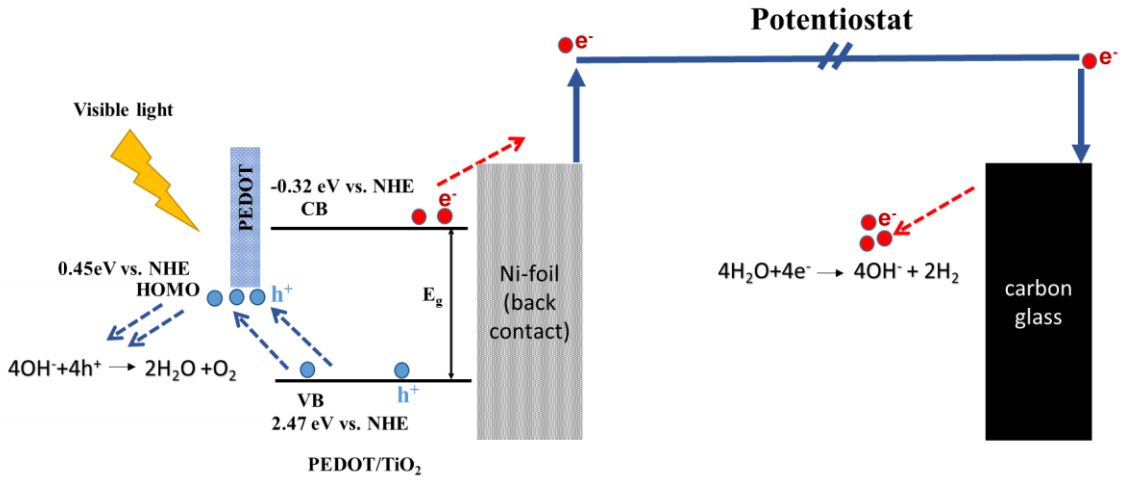

Figure 9. Band structure and charge-transfer mechanism of T85P under irradiation for photo-electro oxidation of water.

4. Conclusion

In this work, innovative PEDOT/TiO_2 photo-anodes were prepared by sequentially depositing anatase TiO_2 films of variable thickness by MOCVD, then PEDOT by oCVD. Increasing TiO_2 thickness from 474 to 2133 nm results in morphological changes, namely from dense and angular structures to complex isolated and nanostructured tree-like columns with prevailing high energy [211] facets. Concomitantly, the surface roughness Ra increases from 9 to 28 nm and the band gap decreases from 3.32 to 2.71 eV. The presence of PEDOT enhances the optical and electrical conductivity properties of the films; the broadest difference is observed for T85 (bare TiO_2) and T85P (PEDOT/TiO_2) as the current in T85P is three orders of magnitude higher than T85 (nano-ampere vs pico-ampere), whereas the applied voltage is two orders of magnitude lower, leading to significant improvement of charge electron transfer, detected by EIS. Moreover, the 1350 nm thick T85P sample shows the highest photocurrent response (0.26 mA cm^{-2} at 1.8 V/RHE), and the fastest photocurrent

response under illumination with e^-/h^+ stability up to 64 ms average time before recombination. The photocurrent value of T85P is approximately 1.8 times higher than that of the bare TiO_2 film with equivalent thickness (T85), indicating a significant enhancement of the photo-generated electrons and holes due to PEDOT layer. This synergetic effect between PEDOT and TiO_2 enhances the hydrogen yield up to 4.1 µmole cm^{-2} h^{-1} (twice that of TiO_2 alone). Such innovative PEDOT/TiO_2 p-n junction prepared by MOCVD and oCVD opens new prospects for PEC cell. H_2 evolution coupling with water remediation is in progress.

5. Acknowledgment

This research was funded by the "Programme opérationnel FEDER-FSE Midi-Pyrénées et Garonne 2014-2020" in the project FEDER REACT EU H2VERT [n°210855FE H2VERT].

6. References

[1] A. A. Nada, M. F. Bekheet, R. Viter, P. Miele, S. Roualdes, M. Bechelany, BN/$Gd_xTi_{(1-x)}O_{(4-x)/2}$ nanofibers for enhanced photocatalytic hydrogen production under visible light, Appl. Catal. B Environ. 251, 2019, 76-86. https://doi.org/10.1016/j.apcatb.2019.03.043.

[2] H. H. El-Maghrabi, A. A. Nada, M. F. Bekheet, S. Roualdes, W. Riedel, I. Iatsunskyi, E. Coy, A. Gurlo, M. Bechelany, Atomic layer deposition of Pd nanoparticles on self-supported carbon-Ni/NiO-Pd nanofiber electrodes for electrochemical hydrogen and oxygen evolution reactions, J. Colloid Interface Sci. 569, 2020, 286-297. https://doi.org/10.1016/j.jcis.2020.02.063.

[3] J. Lin, X. Han, S. Liu, Y. Lv, X. Li, Y. Zhao, Y. Li, L. Wang, S. Zhu, Nitrogen-doped cobalt-iron oxide cocatalyst boosting photoelectrochemical water splitting of $BiVO_4$ photoanodes, Appl. Catal. B Environ. 320, 2023, 121947. https://doi.org/10.1016/j.apcatb.2022.121947.

[4] V. D. Dang, T. Annadurai, A. P. Khedulkar, J.-Y. Lin, J. Adorna, W.-J. Yu, B. Pandit, T.V. Huynh, R.-A. Doong, S-scheme N-doped carbon dots anchored g-C_3N_4/Fe_2O_3 shell/core composite for photoelectrocatalytic trimethoprim degradation and water splitting, Appl. Catal. B Environ. 320, 2023, 121928.

https://doi.org/10.1016/j.apcatb.2022.121928.

[5] Y. Li, S. Tang, H. Sheng, C. Li, H. Li, B. Dong, L. Cao, Multiple roles for LaFeO3 in enhancing the Photoelectrochemical performance of WO_3, J. Colloid Interface Sci. 629, 2023, 598-609. https://doi.org/10.1016/j.jcis.2022.09.090.

[6] H. Zhou, J. Ke, D. Xu, J. Liu, $MnWO_4$ nanorods embedded into amorphous MoS_x microsheets in 2D/1D $MoS_x/MnWO_4$ S–scheme heterojunction for visible-light photocatalytic water oxidation, J. Mater. Sci. Technol. 136, 2023, 169-179. https://doi.org/10.1016/j.jmst.2022.07.021.

[7] C. Tuc Altaf, O. Coskun, A. Kumtepe, M. Sankir, N. Demirci Sankir, Bifunctional ZnO nanowire/$ZnSnO_3$ heterojunction thin films for photoelectrochemical water splitting and photodetector applications, Mater. Lett. 322, 2022, 132450. https://doi.org/10.1016/j.matlet.2022.132450.

[8] A. Ahmad, F. Tezcan, G. Yerlikaya, Zia-ur-Rehman, H. Paksoy, G. Kardaş, Solar light driven photoelectrochemical water splitting using Mn-doped CdS quantum dots sensitized hierarchical rosette-rod TiO_2 photoanodes, J. Electroanal. Chem. 916, 2022, 116384. https://doi.org/10.1016/j.jelechem.2022.116384.

[9] C. Wang, Q.-Q. Hu, J.-Q. Huang, Z.-H. Deng, H.-L. Shi, L. Wu, Z.-G. Liu, Y.-G. Cao, Effective water splitting using N-doped TiO_2 films: Role of preferred orientation on hydrogen production, Int. J. Hydrogen Energy 39, 2014, 1967-1971. https://doi.org/10.1016/j.ijhydene.2013.11.097.

[10] J. Xu, L.-F. Xu, J.-T. Wang, A. Selloni, in: M. Janus (Ed.), Titanium Dioxide IntechOpen, London, England, 2017, Ch. 1.

[11] F. Ullah, R. Bashiri, N. Muti Mohamed, A. Zaleska-Medynska, C. F. Kait, U. Ghani, M. U. Shahid, M.S.M. Saheed, Exploring graphene quantum dots@TiO_2 rutile (0 1 1) interface for visible-driven hydrogen production in photoelectrochemical cell: Density functional theory and experimental study, Appl. Surf. Sci. 576, 2022, 151871. https://doi.org/10.1016/j.apsusc.2021.151871.

[12] A.A. Nada, W. M. A. El Rouby, M. F. Bekheet, M. Antuch, M. Weber, P. Miele, R. Viter, S. Roualdes, P. Millet, M. Bechelany, Highly textured boron/nitrogen co-doped TiO_2 with honeycomb structure showing enhanced visible-light photoelectrocatalytic

activity, Appl. Surf. Sci. 505, 2020, 144419. https://doi.org/10.1016/j.apsusc.2019.144419.

[13] S. Abdelnasser, G. Park, H. Han, R. Toth, H. Yoon, Enhanced photocatalytic performance of poly(3,4-ethylenedioxythiophene)-coated TiO_2 nanotube electrodes, Synth. Met. 251, 2019, 120-126. https://doi.org/10.1016/j.synthmet.2019.03.018.

[14] A. Miquelot, O. Debieu, V. Rouessac, C. Villeneuve, N. Prud'Homme, J. Cure, V. Constantoudis, G. Papavieros, S. Roualdes, C. Vahlas, TiO_2 nanotree films for the production of green H_2 by solar water splitting: From microstructural and optical characteristics to the photocatalytic properties, Appl. Surf. Sci. 494, 2019, 1127-1137. https://doi.org/10.1016/j.apsusc.2019.07.191.

[15] A. Miquelot, L. Youssef, C. Villeneuve-Faure, N. Prud'Homme, N. Dragoe, A. Nada, V. Rouessac, S. Roualdes, J. Bassil, M. Zakhour, In-and out-plane transport properties of chemical vapor deposited TiO_2 anatase films, J. Mater. Sci. 56, 2021, 10458-10476. https://doi.org/10.1007/s10853-021-05955-6.

[16] N. Bashirom, W.K. Tan, G. Kawamura, A. Matsuda, Z. Lockman, Formation of self-organized ZrO_2–TiO_2 and $ZrTiO_4$–TiO_2 nanotube arrays by anodization of Ti–40Zr foil for Cr(VI) removal, J. Mater. Res. Technol. 19, 2022, 2991-3003. https://doi.org/10.1016/j.jmrt.2022.06.055.

[17] L. Zhang, J. Guo, B. Hao, H. Ma, WO_3/TiO_2 heterojunction photocatalyst prepared by reactive magnetron sputtering for Rhodamine B dye degradation, Opt. Mater. (Amst). 133, 2022, 113035. https://doi.org/10.1016/j.optmat.2022.113035.

[18] K. Pham, S. Pelisset, N. Kinnunen, P. Karvinen, T. K. Hakala, J. J. Saarinen, Controlled photocatalytic activity of TiO_2 inverse opal structures with atomic layer deposited (ALD) metal oxide thin films, Mater. Chem. Phys. 277, 2022, 125533. https://doi.org/10.1016/j.matchemphys.2021.125533.

[19] M. Ghorbanloo, A. A. Nada, H. H. El-Maghrabi, M. F. Bekheet, W. Riedel, B. Djamel, R. Viter, S. Roualdes, F.S. Soliman, Y. M. Moustafa, P. Miele, M. Bechelany, Superior efficiency of BN/Ce_2O_3/TiO_2 nanofibers for photocatalytic hydrogen generation reactions, Appl. Surf. Sci. 594, 2022, 153438. https://doi.org/10.1016/j.apsusc.2022.153438.

[20] M. Lal, P. Sharma, C. Ram, Synthesis and photocatalytic potential of Nd-doped TiO_2 under UV and solar light irradiation using a sol-gel ultrasonication method, Results Mater. 15, 2022, 100308. https://doi.org/10.1016/j.rinma.2022.100308.

[21] R. T. Bento, O. V. Correa, R. A. Antunes, M. F. Pillis, Surface properties enhancement by sulfur-doping TiO_2 films, Mater. Res. Bull. 143, 2021, 111460. https://doi.org/10.1016/j.materresbull.2021.111460.

[22] Z. Katančić, W.-T. Chen, G. I. N. Waterhouse, H. Kušić, A. Lončarić Božić, Z. Hrnjak-Murgić, J. Travas-Sejdic, Solar-active photocatalysts based on TiO_2 and conductive polymer PEDOT for the removal of bisphenol A, J. Photochem. Photobiol. A Chem. 396, 2020, 112546. https://doi.org/10.1016/j.jphotochem.2020.112546.

[23] K. Su, N. Nuraje, L. Zhang, I. Chu, R. M. Peetz, H. Matsui, N. Yang, Fast Conductance Switching in Single-Crystal Organic Nanoneedles Prepared from an Interfacial Polymerization-Crystallization of 3,4-Ethylenedioxythiophene, Adv. Mater. 19, 2007, 669-672. https://doi.org/10.1002/adma.200602277.

[24] M. Mirabedin, H. Vergnes, N. Caussé, C. Vahlas, B. Caussat, Liquid antimony pentachloride as oxidant for robust oxidative chemical vapor deposition of poly(3,4-ethylenedioxythiophene) films, Appl. Surf. Sci. 554, 2021, 149501. https://doi.org/10.1016/j.apsusc.2021.149501.

[25] H. Xu, X. Zhao, G. Yang, X. Ji, X. Zhang, L. Li, B. Wu, X. Ouyang, Y. Ni, L. Chen, H.-C. Hu, Modification of PEDOT:PSS towards high-efficiency OLED electrode via synergistic effect of carboxy and phenol groups from biomass derivatives, Chem. Eng. J. 430, 2022, 133014. https://doi.org/10.1016/j.cej.2021.133014.

[26] R. Hermi, M. Mahdouani, R. Bourguiga, S. Mahato, Modelling and simulation of the electrical parameters of DMSO doped PEDOT: PSS/n-Si organic/inorganic solar cells using the Lambert W function, Micro and Nanostructures 168, 2022, 207258. https://doi.org/10.1016/j.micrna.2022.207258.

[27] M. J. Salar-Garcia, F. Montilla, C. Quijada, E. Morallon, I. Ieropoulos, Improving the power performance of urine-fed microbial fuel cells using PEDOT-PSS modified anodes, Appl. Energy 278, 2020, 115528. https://doi.org/10.1016/j.apenergy.2020.115528.

[28] Y. Che, H. Zhang, T. Abdiryim, R. Jamal, A. Kadir, Z. Helil, H. Liu, Ultraviolet photodetectors based on TiO_2 nanorod arrays/PEDOT-type conducting polymers, Opt. Mater. (Amst) 122, 2021, 111805. https://doi.org/10.1016/j.optmat.2021.111805.

[29] J. Liu, D. L. McCarthy, L. Tong, M. J. Cowan, J. M. Kinsley, L. Sonnenberg, K. H. Skorenko, S. M. Boyer, J. B. DeCoste, W. E. Bernier, Poly (3,4-ethylenedioxythiophene)(PEDOT) infused TiO_2 nanofibers: The role of hole transport layer in photocatalytic degradation of phenazopyridine as a pharmaceutical contaminant, Rsc Adv. 6, 2016, 113884. https://doi.org/10.1039/C6RA22797J.

[30] K. Siuzdak, M. Szkoda, A. Lisowska-Oleksiak, J. Karczewski, J. Ryl, Highly stable organic–inorganic junction composed of hydrogenated titania nanotubes infiltrated by a conducting polymer, RSC Adv. 6, 2016, 33101. https://doi.org/ 10.1039/C6RA01986B.

[31] B. Gao, J. An, Y. Wang, L. Wang, M. Sillanpää, Comparative study of the photocatalytic, electrocatalytic and photoelectrocatalytic behaviour of poly (3,4-ethylenedioxythiophene), J. Electroanal. Chem. 858, 2020, 113742. https://doi.org/10.1016/j.jelechem.2019.113742.

[32] X. Zhu, X. Han, R. Guo, P. Yuan, L. Dang, Z. Liu, Z. Lei, Vapor-phase polymerization of fibrous PEDOT on carbon fibers film for fast pseudocapacitive energy storage, Appl. Surf. Sci. 597, 2022, 153684. https://doi.org/10.1016/j.apsusc.2022.153684.

[33] M. Mirabedin, H. Vergnes, N. Caussé, C. Vahlas, B. Caussat, An out of the box vision over oxidative chemical vapor deposition of PEDOT involving sublimed iron trichloride, Synth. Met. 266, 2020, 116419. https://doi.org/10.1016/j.synthmet.2020.116419.

[34] G. Drewelow, H. W. Song, Z.-T. Jiang, S. Lee, Factors controlling conductivity of PEDOT deposited using oxidative chemical vapor deposition, Appl. Surf. Sci. 501, 2020, 144105. https://doi.org/10.1016/j.apsusc.2019.144105.

[35] J. Rodríguez-Carvajal, Recent Developments of the Program FULLPROF, in: Commission on Powder Diffraction (IUCr). Newsletter 26, 2001, 12-19.

[36] L. W. Finger, D. E. Cox, A. P. Jephcoat, A Correction for Powder Diffraction Peak

Asymmetry Due to Axial Divergence, J. Appl. Crystallogr. 27, 1994, 892-900. http://dx.doi.org/10.1107/S0021889894004218.

[37] W. A. Dollase, Correction of intensities for preferred orientation in powder diffractometry: application of the March model, J. Appl. Crystallogr. 19, 1986, 267-272. https://doi.org/10.1107/S0021889886089458.

[38] E. Zolotoyabko, Determination of the degree of preferred orientation within the March–Dollase approach, J. Appl. Crystallogr. 42, 2009, 513-518. https://doi.org/10.1107/S0021889809013727.

[39] A. A. Nada, M. Nasr, R. Viter, P. Miele, S. Roualdes, M. Bechelany, Mesoporous $ZnFe_2O_4$@TiO_2 Nanofibers Prepared by Electrospinning Coupled to PECVD as Highly Performing Photocatalytic Materials, J. Phys. Chem. C. 121, 2017, 24669-24677. https://doi.org/10.1021/acs.jpcc.7b08567.

[40] C. Sarantopoulos, Photocatalyseurs à base de TiO_2 préparés par infiltration chimique en phase vapeur (CVI) sur supports microfibreux, Master Thesis, INP Toulouse, 2007.

[41] P. Tyagi, A. G. Vedeshwar, Optical properties of ZnI_2 films, Phys. Rev. B. 64, 2001, 245406. https://doi.org/10.1103/PhysRevB.64.245406.

[42] P. Kumar, V. Gulia, A. G. Vedeshwar, Residual stress dependant anisotropic band gap of various (hkl) oriented BaI_2 films, J. Appl. Phys. 114, 2013, 193511. http://dx.doi.org/10.1063/1.4832437.

[43] S. Kawrani, A. A. Nada, M. F. Bekheet, M. Boulos, R. Viter, S. Roualdes, P. Miele, D. Cornu, M. Bechelany, Enhancement of calcium copper titanium oxide photoelectrochemical performance using boron nitride nanosheets, Chem. Eng. J. 389, 2020, 124326. https://doi.org/10.1016/j.cej.2020.124326.

[44] A. Barhoum, H. H. El-Maghrabi, A. A. Nada, S. Sayegh, A. Renard, S. Roualdes, I. Iatsunskyi, E. Coy, M. Bechelany, Simultaneous hydrogen and oxygen evolution reactions using free-standing nitrogen-doped-carbon-Co/CoO_x nanofiber electrodes decorated with palladium nanoparticles, J. Mater. Chem. A. 9, 2021, 17724. https://doi.org/10.1039/D1TA03704H.

[45] S. Kawrani, M. Boulos, M. F. Bekheet, R. Viter, A. A. Nada, W. Riedel, S. Roualdes, D. Cornu, M. Bechelany, Segregation of copper oxide on calcium copper titanate

surface induced by Graphene Oxide for Water splitting applications, Appl. Surf. Sci. 516, 2020, 146051. https://doi/org/10.1016/j.apsusc.2020.146051.

[46] A. A. Nada, W. M. A. El Rouby, M. F. Bekheet, M. Antuch, M. Weber, P. Miele, R. Viter, S. Roualdes, P. Millet, M. Bechelany, Highly textured boron/nitrogen co-doped TiO_2 with honeycomb structure showing enhanced visible-light photoelectrocatalytic activity, Appl. Surf. Sci. 505, 2020, 144419. https://doi.org/10.1016/j.apsusc.2019.144419.

[47] S. V. Singh, U. Gupta, S. Biring, B. Mukherjee, B. N. Pal, In-situ grown nanoscale p-n heterojuction of Cu_2S-TiO_2 thin film for efficient photoelectrocatalytic H_2 evolution, Surfaces and Interfaces 28, 2022, 101660. https://doi.org/https://doi.org/10.1016/j.surfin.2021.101660.

[48] M. P. Kobylański, A. Tercjak, H. Remita, X. Yuan, O. Cavdar, J. Gutierrez, A. Zaleska-Medynska, A Pedot-Pt-TiO_2 Hybrid Material Synthesized by the Casting Method for Photocatalytic Hydrogen Generation, Available SSRN 4223078. (n.d.).

[49] Q. Shao, H. Lin, M. Shao, Determining Locations of Conduction Bands and Valence Bands of Semiconductor Nanoparticles Based on Their Band Gaps, ACS Omega 5, 2020, 10297-10300. https://dx.doi.org/10.1021/acsomega.9b04238?ref=pdf.

[50] M. Bledowski, L. Wang, A. Ramakrishnan, O. V Khavryuchenko, V. D. Khavryuchenko, P. C. Ricci, J. Strunk, T. Cremer, C. Kolbeck, R. Beranek, Visible-light photocurrent response of TiO_2–polyheptazine hybrids: evidence for interfacial charge-transfer absorption, Phys. Chem. Chem. Phys. 13, 2021, 21511-21519. https://doi.org/ 10.1039/c1cp22861g.

[51] J. Zhang, P. Zhou, J. Liu, J. Yu, New understanding of the difference of photocatalytic activity among anatase, rutile and brookite TiO_2, Phys. Chem. Chem. Phys. 16, 2014, 20382-20386. https://doi.org/10.1039/c4cp02201g.

[52] M. M. Tavakoli, M. H. Gharahcheshmeh, N. Moody, M. G. Bawendi, K. K. Gleason, J. Kong, Efficient, Flexible, and Ultra-Lightweight Inverted PbS Quantum Dots Solar Cells on All-CVD-Growth of Parylene/Graphene/oCVD PEDOT Substrate with High Power-per-Weight, Adv. Mater. Interfaces 7, 2020, 2000498. https://doi.org/10.1002/admi.202000498.